RSC Advances

PAPER

View Article Online
View Journal | View Issue

Cite this: *RSC Adv.*, 2025, **15**, 15443

N-doped carbon/$Ti_3C_2T_x$ MXene free-standing films as sulfur hosts for Li–S batteries†

Renzhong Hou,‡[ab] Haoyu Bai,‡[a] Xiongwei Zhong,[a] Jiaji Cheng,*[c] Jie Gao,[d] Jun Tang*[b] and Baomin Xu*[a]

Received 10th March 2025
Accepted 26th April 2025

DOI: 10.1039/d5ra01727k

rsc.li/rsc-advances

The performance of sulfur-based cathodes is restricted by the poor conductivity of sulfur and the shuttle effect of lithium polysulfides (LiPSs). Herein, an effective N-doped carbon/$Ti_3C_2T_x$ (NC/$Ti_3C_2T_x$) free-standing architecture was designed as a sulfur host for achieving high sulfur loadings, considerable electronic conductivity and good LiPS trapping ability to suppress the shuttle effect. Consequently, an excellent electrochemical performance was achieved for the NC-S/$Ti_3C_2T_x$ freestanding structure with a 38% increase in capacity compared with the counterpart electrode of slurry-coated NC-S/$Ti_3C_2T_x$. Moreover, the NC-S/$Ti_3C_2T_x$ freestanding structure exhibits a high capacity of 1156 mA h g^{-1} at 0.1C and a high capacity retention of 79.5% after 100 cycles. Moreover, this architecture enabled high sulfur loadings, and thus, a high areal capacity of 3.41 mA h cm^{-2} was obtained.

Introduction

Rapidly growing demands for efficient and economical energy storage devices promote the development of rechargeable batteries. The state-of-the-art lithium-ion batteries (LIBs) are approaching the energy-density limitation and are not sufficiently powerful for next-generation devices. Lithium–sulfur batteries, with pollution-free and low-cost sulfur-based cathodes, have been attracting increasing interests in recent years owing to their high theoretical specific capacity of up to 1675 mA h g^{-1} and a theoretical specific energy density of 2600 W h kg^{-1}.[1,2] However, the low conductivity of sulfur, the shuttle effect of lithium polysulfides (LiPSs) and the volume expansion during charge/discharge have greatly restricted the electrochemical performance of lithium–sulfur batteries.[3–6] Ideally, effective hosts for sulfur loading should be electrochemically and mechanically stable to resist the volume expansion and should be conductive. Moreover, strong polar sites should be introduced for anchoring LiPSs during the charge–discharge process to alleviate the shuttle effect. Frameworks based on graphenes,[7–9] carbon nanotubes,[10–12] and metal–organic frameworks (MOFs)[13] have been extensively reported. However, the weak interaction between LiPSs and carbon materials results in a severe shuttle effect. Nitrogen-doped carbon materials with relatively strong polar sites can be used as sulfur hosts for preventing the LiPS diffusion.[14–18] However, their short-range and long-range electronic conductivities are relatively low.

MXenes ($M_{n+1}X_nT_x$, where T represents the surface groups including = O, –F and –OH), a family of 2D materials, have attracted great interest in energy storage fields.[19–24] $Ti_3C_2T_x$, which is the first reported and most studied MXene, has been extensively reported as a sulfur host owing to its high electrical conductivity (>15 000 S cm^{-1}), considerable mechanical strength and tunable surface terminations.[25–31] To fully utilize the advantages of the high conductivity of $Ti_3C_2T_x$ and the strong polar sites of carbon nitrides, herein, a free-standing film electrode comprising sulfur-infused nitrogen-doped carbon embedded in $Ti_3C_2T_x$ nanosheets (NC–S/$Ti_3C_2T_x$) is reported.[32] On the one hand, the highly conductive $Ti_3C_2T_x$ network provided electronic conduction "highways", which ensured the full utilization and enabled the fast electrochemical reaction of sulfur electrodes.[33–36] On the other hand, nitrogen doping introduced local strong polar regions in carbon materials. These polar sites interacted strongly with S^- or Li^+ in LiPSs to form S–N or Li–N bonds, which enhanced the adsorption capacity and effectively avoided the shuttle effect compared with undoped materials.[37–41] Moreover, NC-S was wrapped between $Ti_3C_2T_x$ nanosheets, which further prevented the diffusion of LiPSs and adapted to the volume expansion. Compared to reported strategies, this strategy avoided the preparation of slurry for scraping, and the preparation process was simpler. Furthermore, as this strategy does not require additional conductive carbon black and binders (such as PVDF),

[a]*Department of Materials Science and Engineering, Southern University of Science and Technology, Shenzhen 518055, China. E-mail: xubm@sustech.edu.cn*

[b]*College of New Materials and New Energy, Shenzhen Technology University, Shenzhen, Guangdong 518118, China. E-mail: tangjun3@sztu.edu.cn*

[c]*School of Materials Science and Engineering, Hubei University, Wuhan, 430062, China. E-mail: jiajicheng@hubu.edu.cn*

[d]*IC Seal Co Ltd, Shanghai, 2001202, China*

† Electronic supplementary information (ESI) available. See DOI: https://doi.org/10.1039/d5ra01727k

‡ These authors contributed equally to this work.

compared with the traditional slurry process, this approach ensured the conductivity of the electrode along with improving the proportion of sulfur.[42,43] Accordingly, the NC-S/$Ti_3C_2T_x$ free-standing cathode exhibited significantly improved electrochemical performances in terms of cycling life, rate capability, and charge transfer resistance, with high sulfur loadings.

Results and discussion

The preparation of a free-standing NC-S/$Ti_3C_2T_x$ film is schematically illustrated in Fig. 1 (experimental details are provided in the ESI†). Hydrothermally synthesized NC spheres were used as hosts for sulfur loading due to their porous structure formed during the carbonization process.[44,45] Besides, nitrogen doping in the cracks of NC by the pyrogenic decomposition of melamine created strong C–N polar anchoring sites.[46] At 155 °C, the molten sulfur diffused into the defects of the as-obtained NC to form NC-S.[47] The NC spheres were small in diameter (2 to 10 μm, shown in Fig. S1†), and hence, they were easily encapsulated in free-standing hybrids formed by the $Ti_3C_2T_x$ intersecting sheets, ensuring the structural stability as the sulfur reservoir. Upon vacuum filtration of the solution of monolayer $Ti_3C_2T_x$ MXene colloidal and NC-Ss, followed by a freeze-drying procedure, a free-standing NC-S/$Ti_3C_2T_x$ film was obtained.

In order to indicate the surface morphology of the free-standing NC-S/Ti_3C_2Tx film, SEM characterizations were performed. In the microscopic view, the as-obtained NCs exhibited very rough surfaces and inner sections after the hydrothermal reaction and annealing (Fig. 2a and S2a†), which is beneficial to a higher sulfur loading and abundant adhesion sites. After sulfur loading, the sulfur infusion leveled some of the trenches that made the NC-S surface smoother than NC (Fig. 2b). Due to the relatively weak sulfur fixation by NC alone, a duplicate protection mechanism is needed outside of the NC-S.[48] That is, nitrogen-doped porous carbon is used as a sulfur carrier (NC-S), MXene nanosheets are used to wrap NC-S, and LiPSs are adsorbed by the rich surface groups of MXenes to achieve further sulfur fixation. Fig. S2b and S2c† reveal how NC-S was

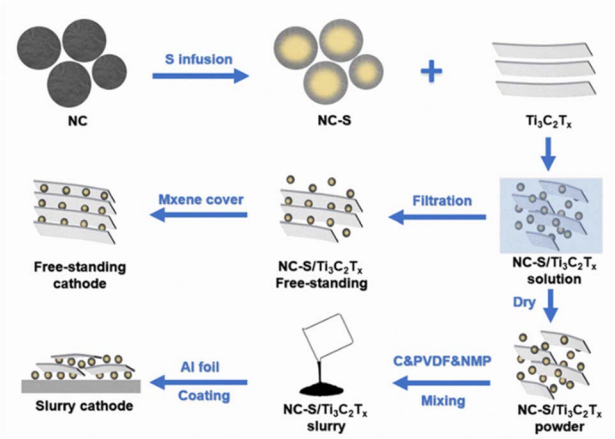

Fig. 1 Schematic of the fabrication of slurry coating and free-standing NC-S/$Ti_3C_2T_x$ MXene hybrids.

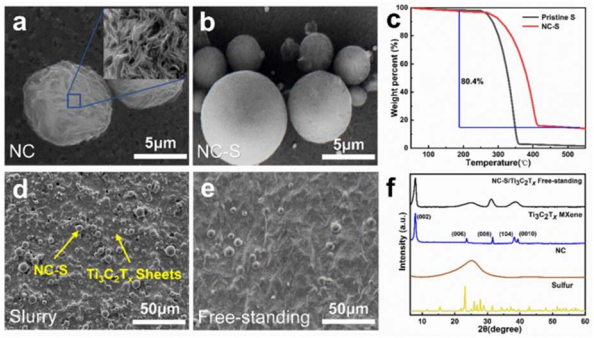

Fig. 2 SEM images of (a) NC and (b) NC-S, (c) TG curves of S and NC-S. SEM images of (d) NC-S/$Ti_3C_2T_x$ slurry and (e) free-standing NC-S/$Ti_3C_2T_x$ film. (f) XRD patterns of sulfur, NC, $Ti_3C_2T_x$ MXene and free-standing NC-S/$Ti_3C_2T_x$.

locked in $Ti_3C_2T_x$ MXene cross-bedding structures. Compared with the NC-S/$Ti_3C_2T_x$ slurry, more homogeneous $Ti_3C_2T_x$ MXene sheets on the film surface (shown in Fig. 2d and e) provide a stronger encapsulation of NC-S. On the one hand, the dense MXene sheet can physically block the shuttle of lithium polysulfides; on the other hand, it can also rely on the rich surface groups of MXenes to chemically adsorb lithium polysulfides. Compared with NC alone, the sulfur fixation effect is more significant.

Nitrogen adsorption/desorption isotherm measurements were implemented to analyze the surface properties and the pore size distribution. As shown in Fig. S3a,† The NC owns a type IV isotherm with a small hysteresis loop, showing numerous macro- and micro-pores on NCs. The BET measurements presented in Table S1† illustrate that NCs have a large specific surface area up to 489 $m^2\ g^{-1}$ and a high pore volume of 1.69 $cm^3\ g^{-1}$ that guarantee a high sulfur loading. The HK model was employed to calculate the pore size distribution of the slit voids on the NC surface. The plot shown in Fig. S3b† indicates that the slit diameters are mostly between 0.5 and 0.8 nanometers in size, proving the existence of abundant nano-scaled micropores, which are beneficial for strengthening the restraining of LiPSs.[49] Thermogravimetric Analysis shown in Fig. 2c reveals that the sulfur loading factor of NC-S is 80.4%, which is at a high level compared with the traditional carbon-based host (generally 70%),[50] and consequently, the sulfur weight content of the prepared free-standing NC-S/$Ti_3C_2T_x$ film is 60.5%. In addition, due to the fixation of sulfur, the sulfur in NC-S has a higher initial decomposition temperature and end temperature, and shows better thermal stability as a whole.

The as-prepared material crystal structure was investigated by XRD. As shown in Fig. 2f, the peaks at 7.9°, 23.7°, 31.6° and 39.5° display the restacking 2D nature of the $Ti_3C_2T_x$ MXene (corresponding to the crystal faces of (002), (006), (008), and (0010), respectively).[51] However, the peaks that refer to sulfur are quite grading because the original crystalline sulfur (S8) became amorphous during the melt infusion penetration process. This plot also indicates that there is almost no residual sulfur on the film surface.

The corresponding EDS elemental mapping of NC (Fig. S4†) illustrates the uniform nitrogen doping of NC. Moreover, the EDS elemental mapping indicates the uniform sulfur attachment to the shallow voids, as shown in Fig. 3f. Similar to what SEM displayed, weaker signals shown in Fig. 3l than in Fig. 3i confirm that fewer sulfur-containing particles exist on the free-standing film surface owing to better sulfur immobilization.[52]

To exclusively evaluate the electrochemical performance of the prepared NC-S/$Ti_3C_2T_x$ cathodes, a series of tests were conducted. Fig. 4a presents the cyclic voltammetry results of lithium–sulfur batteries with the NC-S/$Ti_3C_2T_x$ slurry cathode and free-standing NC-S/$Ti_3C_2T_x$ cathode. For the simple mixture slurry cathode, two evident reduction peaks can be found at 1.95 V and 2.25 V that are attributed to the reduction from S_8 to LiPSs (Li_2S_n, $4 \leq n \leq 8$) and a second reduction to Li_2S or Li_2S_2.[53] Inversely, the oxidation peak at about 2.48 V corresponds to the multi-stage oxidation of Li_2S/Li_2S_2 to LiPSs and sulfur. The reduction peaks of the free-standing cathode slightly increase (0.03 V), while the oxidation peak decreases (0.01 V) compared with the NC-S/$Ti_3C_2T_x$ slurry cathode.[54] This is due to the addition of large-area MXene nanosheets and there is no need to use insulating materials such as binders. The conductivity of the electrode is greatly improved compared to the traditional slurry, thereby improving the kinetics of the redox reaction and improving the reversibility of the reaction.

Fig. 4b shows the cycling performance between NC-S/$Ti_3C_2T_x$ slurry and free-standing NC-S/$Ti_3C_2T_x$ cathodes. Their initial reversible specific capacities are 1240 mA h g^{-1} and 1156 mA h g^{-1} (because the NC-S/$Ti_3C_2T_x$ slurry cathode owns lower sulfur percentage caused by the addition of conductive carbon and PVDF, at 48.4%). After 100 charge and discharge cycles at 0.1C, 57.7% and 79.5% of capacities at 715 mA h g^{-1} and 919 mA h g^{-1} were retained, respectively. The free-standing NC-S/$Ti_3C_2T_x$ cathode, with a fading rate at 0.21% represents

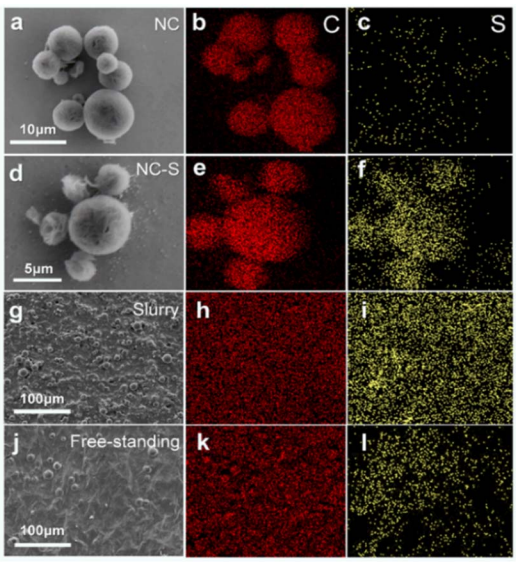

Fig. 3 SEM images and EDS mappings of C and S of (a–c) NC before sulfur infusion, (d–f) NC-S, (g–i) NC-S/$Ti_3C_2T_x$ slurry and (j–l) the free-standing NC-S/$Ti_3C_2T_x$ film.

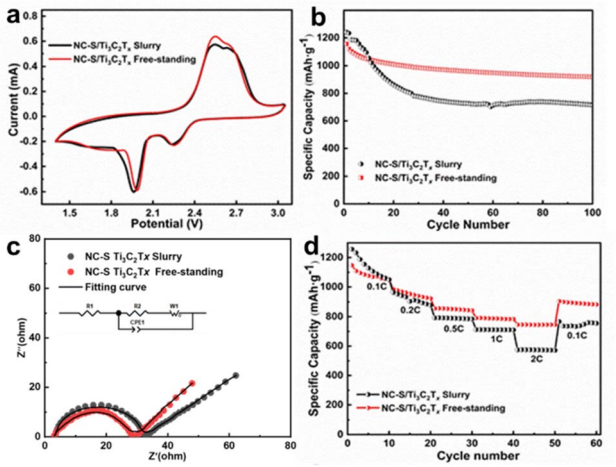

Fig. 4 Electrochemical characterization of the as-prepared Li–S cells. (a) CV profiles of lithium–sulfur cells with NC-S/$Ti_3C_2T_x$ slurry/free-standing NC-S/$Ti_3C_2T_x$ cathodes. (b) Cycling performance at 0.1C of lithium–sulfur cells with the NC-S/$Ti_3C_2T_x$ slurry and free-standing NC-S/$Ti_3C_2T_x$ cathodes at 1.2 mg cm^{-2} sulfur loading. (c) Nyquist plots of the lithium–sulfur cells with the NC-S/$Ti_3C_2T_x$ slurry and NC-S/$Ti_3C_2T_x$ free-standing cathodes. (d) Rate performance of the lithium–sulfur cells with the NC-S/$Ti_3C_2T_x$ slurry and free-standing NC-S/$Ti_3C_2T_x$ cathodes.

better cycling performance, demonstrating its excellent cycling stability. These results match the charge and discharge plateaus well in Fig. S5,† and the free-standing one shows more distinct and flatter plateaus during the cycles. In Fig. S6,† the coulombic efficiency shows a slight increase during the first ten cycles due to the unstable LiPS dissolution after original cycles, and through comparison, the free-standing network does not affect the coulombic efficiency.[55] Fig. 4c shows the Electrochemical Impedance Spectroscopy (EIS) test plots. According to the figure, the charge transfer resistance (R_{ct}) values of the free-standing cathodes (25.6 Ω) are lower than those of the slurry cathodes (29.5 Ω) because of the excellent conductivity of the more regular free-standing NC/$Ti_3C_2T_x$ network. In addition, the smaller arc area at high frequencies accounts for a more robust redox reaction and the curve with a higher slope in the low-frequency zones indicates easier ion diffusion into the free-standing cathode, which strengthens the rate capacities of batteries.[50]

The rate capabilities of the NC-S/$Ti_3C_2T_x$ slurry and free-standing film cathodes are shown in Fig. 4d. Better reversible capacities of 1150, 985, 856, 791 and 746 mA h g^{-1} were obtained at 0.1C, 0.2C, 0.5C, 1C and 2C with the free-standing cathode. In contrast, the capacity drop of the NC-S/$Ti_3C_2T_x$ slurry cathode-based cell is more pronounced, especially under a heavy current. Therefore, the capacity reservation of the free-standing NC-S/$Ti_3C_2T_x$ cathode during the current density switch to 2C (64.9%) and back to 0.1C (82.4%) was larger than what NC-S/$Ti_3C_2T_x$ slurry cathode possesses (47.0% and 64.2%). At the same time, the electrochemical performance of the two electrodes is better than that of the previous electrode with only a single variable (*i.e.*, only adding nitrogen-doped porous carbon or only adding $Ti_3C_2T_x$ MXene), which proves the

synergistic effect of the two materials.[56,57] As shown in Fig. 5a and b, the plateaus drop less for free-standing NC-S/$Ti_3C_2T_x$ cathodes. It means that the two-stage redox reaction continued steadily even at high rates with better refined LiPS shuttle restriction.

Under heavy current and high sulfur loading, the free-standing NC-S/$Ti_3C_2T_x$ electrode still shows excellent cycling performance. At a 2C measurement, as shown in Fig. 5c, the cell delivers a capacity of 624 mA h g^{-1} after 200 cycles, resulting in an average capacity depletion rate of 0.12%. The charge/discharge profiles at 2C of the 1st, 50th, 100th, 150th and 200th cycle shown in Fig. S7† confirm the great capacity reversibility because of the stable charge/discharge plateaus.[36] When the cathodes were fabricated with a sulfur loading of 5 mg cm^{-2}, the initial areal capacity was 3.41 mA h cm^{-2} at 0.5C with a capacity degradation rate of 0.09% over 200 cycles (Fig. 5d). As summarized in Table S2,† the stable LiPS restraining by polar nitrogen and $Ti_3C_2T_x$ network provides a possibility for the preparation of batteries balancing considerable energy density and cycle rate well.

To verify the outstanding chemical durability of the free-standing NC-S/$Ti_3C_2T_x$ structure, electrodes after 200 charge/discharge cycles at 2C were analyzed. In Fig. 6a, there is almost no macroscopic injury on the film surface, and the cathode can still be removed nondestructively from the separator. The SEM view (Fig. 6c) of the cycled cathode shows that the surface of the film remains undamaged, with no NC-Ss scattered, compared with the uncycled films.

The XPS investigations were performed to analyze the surface chemistry change of the NC-S/$Ti_3C_2T_x$ film. The overall

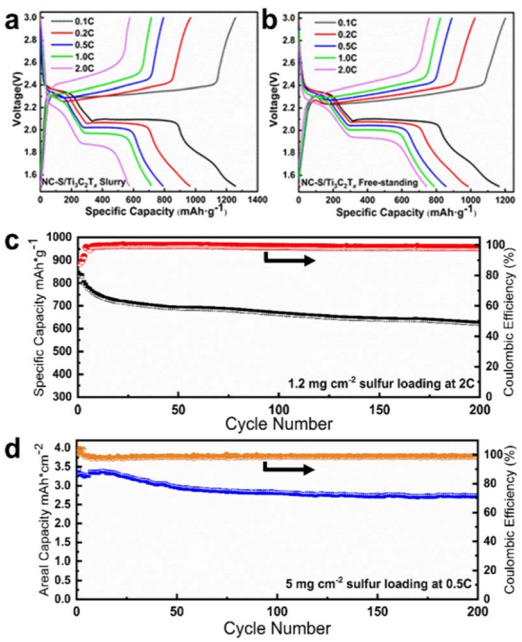

Fig. 5 First discharge and charge curves of (a) NC-S/$Ti_3C_2T_x$ slurry and (b) free-standing NC-S/$Ti_3C_2T_x$ cathodes at different rates. Cycling performance and coulombic efficiency of the free-standing NC-S/$Ti_3C_2T_x$ cathode-based cells (c) at 2C and (d) at 0.5C (5.0 mg cm^{-2} sulfur loading).

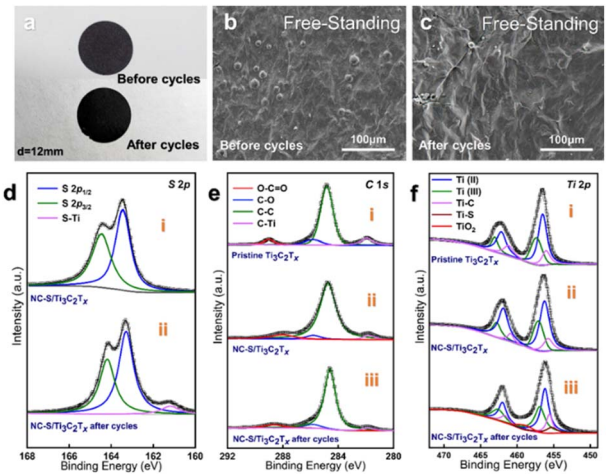

Fig. 6 Comparison of the free-standing NC-S/$Ti_3C_2T_x$ cathodes before and after 200 charge–discharge cycles. (a) Photographs of the cathode films before and after 200 cycles at 2C. SEM image of (b) uncycled and (c) cycled free-standing NC-S/$Ti_3C_2T_x$ films. XPS (d) S 2p spectrum, (e) C 1s spectrum and (f) Ti 2p spectrum of the pristine $Ti_3C_2T_x$ and free-standing NC-S/$Ti_3C_2T_x$ films before and after 200 cycles at 2C.

spectrum indicates that the free-standing film contains mainly C, O, Ti and S (Fig. S8†), and their atomic percentages are 32.36%, 22.93%, 30.99%, and 2.71%, respectively (Table S3†). There are two main peaks: S $2p_{3/2}$ (164.7 eV) and S $2p_{1/2}$ (163.3 eV) in the S 2p high-resolution spectra shown in Fig. 6d. The resolved C 1s and Ti 2p spectra of free-standing NC-S/$Ti_3C_2T_x$ are displayed in Fig. 6e_{ii} and f_{ii}, The C 1s core level was matched with four peaks at 281.8, 284.8, 285.9 and 288.7 eV that could be assigned to C–Ti, C–C, C–O, and O=C–O in the pristine $Ti_3C_2T_x$ MXene. Besides, the Ti 2p plot was fitted with three doublets (Ti $2p_{3/2}$ to Ti $2p_{1/2}$) with a 5.6 eV peak gap and an area ratio of approximately 2 : 1. Signals at 455.5 eV and 461.4 eV are related to Ti–C bonds. Peaks located at 462.7 eV, 461.9 eV, 457.1 eV and 456.0 eV correspond to Ti^{2+} and Ti^{3+} states that are associated with the existence of $Ti_3C_2(OH)_x$ and $Ti_3C_2O_x$. All these factors demonstrate the unoxidized states and chemical interaction of NC-S and $Ti_3C_2T_x$ sheets. After comparing the S 2p XPS surveys before and after cycles in Fig. 6d, the new Ti–S peak (162.8 eV) formation reveals the strong trapping effect (S–Ti–C interaction) between LiPSs and the protective network. The resolved spectra of Ti 2p and C 1s confirm that the free-standing films are preserved well after 200 cycles. We can observe all 4 signals corresponding to carbon-contained bonds in both Fig. 6e_{ii} and e_{iii}. Similarly, the Ti 2p spectrum of the cycled free-standing film shown in Fig. 6f_{iii} also contains all initial peaks. In addition, the relative decrease proportion of C–Ti in the C 1s spectra indicates the breakage of C–Ti bonds after cycles and the increase contribution of titanium oxide due to electrochemical oxidation can also be observed. Furthermore, the cycled Ti 2p spectrum shows an extra signal indicative of Ti–S bonds exactly corresponding to the variation in the S 2p spectra. In conclusion, the almost undamaged free-standing hybrids prove their reliability for sulfur reservoirs.

The superior cycling and rate performances of the free-standing NC-S/$Ti_3C_2T_x$ Li–S batteries are ascribed to the free-standing encapsulation. First, the high electronic conductivity of the NC/$Ti_3C_2T_x$ network remarkably lower the electron transfer resistance, thus improving the sulfur utilization. Second, abundant polar sites of NC and $Ti_3C_2T_x$ MXene can trap the polysulfides well to restrict the shuttle effect. Third, the tight free-standing stacks provide powerful barriers against volumetric expansion, further enhancing the stability performance.

Conclusions

In summary, we have developed a method to fabricate a free-standing NC-S/$Ti_3C_2T_x$ MXene film for Li–S batteries. During synthesis, the nanoscale pores of NC were infused with sulfur, forming a close adhesion. MXene monolayers then wrapped these NC-Ss to constitute an interlaced free-standing composite. The good electronic conductivity of the NC and $Ti_3C_2T_x$ network reduced the electron transfer impedance, thus enhanced the reaction kinetics. With the strong interaction between LiPSs, NC and $Ti_3C_2T_x$ sheets, the free-standing hybrid effectively lowered the lithium polysulfide shuttle in the electrolyte. With these merits, the free-standing NC-S/$Ti_3C_2T_x$ cathodes exhibited outstanding cyclic and rate capacities. This study reported the application of the free-standing NC-S/$Ti_3C_2T_x$ films in Li–S batteries, and they can also be applied in other energy storage devices such as sodium–sulfur batteries.

Data availability

The data supporting this article have been included as part of the ESI.†

Author contributions

R. Hou, J. Tang and B. Xu conceived the ideas and concepts and initiated the research. R. Hou, H. Bai and X. Zhong synthesized the test materials. J. Cheng and J. Gao also conceived the concepts and assisted with the analysis and discussion. R. Hou, J. Cheng J. Tang and B. Xu wrote the manuscript with inputs from all authors.

Conflicts of interest

There are no conflicts to declare.

Acknowledgements

This work was supported by the Shenzhen Science and Technology Innovation Committee (Grant No. JCYJ20220818100406014), SUSTech Energy Institute for Carbon Neutrality (High level of special funds, G03034K001), the National Natural Science Foundation of China (NSFC) (No. 52302294), GuangDong Basic and Applied Basic Research Foundation (No. 2022A1515111140), the Natural Science Foundation of Top Talent of SZTU (No. GDRC202348), the Chinese College Students Innovation and Entrepreneurship Project (Grant No. S201914325031) and the National Natural Science Foundation of Hubei Province (No. 2020CFB200 and 2023AFB635). We would also like to acknowledge the technical support from SUSTech Core Research Facilities.

Notes and references

1 Q. Shao, S. Zhu and J. Chen, A review on lithium-sulfur batteries: Challenge, development, and perspective, *Nano Res.*, 2023, **16**(6), 8097–8138.
2 Y. Fei and G. Li, Unveiling the Pivotal Parameters for Advancing High Energy Density in Lithium-Sulfur Batteries: A Comprehensive Review, *Adv. Funct. Mater.*, 2024, **34**(21), 2312550.
3 Z. Pan, D. J. L. Brett, G. He, *et al.*, Progress and perspectives of organosulfur for lithium–sulfur batteries, *Adv. Energy Mater.*, 2022, **12**(8), 2103483.
4 R. Chen, Y. Zhou and X. Li, Nanocarbon-enabled mitigation of sulfur expansion in lithium–sulfur batteries, *Energy Storage Mater.*, 2024, **68**, 103353.
5 H. Li, S. Ma, J. Li, *et al.*, Altering the reaction mechanism to eliminate the shuttle effect in lithium-sulfur batteries, *Energy Storage Mater.*, 2020, **26**, 203–212.
6 J. Li, L. Gao, F. Pan, *et al.*, Engineering strategies for suppressing the shuttle effect in lithium–sulfur batteries, *Nano-Micro Lett.*, 2024, **16**(1), 12.
7 T. Yang, J. Xia, Z. Piao, *et al.*, Graphene-based materials for flexible lithium–sulfur batteries, *ACS Nano*, 2021, **15**(9), 13901–13923.
8 J. Tian, F. Xing and Q. Gao, Graphene-based nanomaterials as the cathode for lithium-sulfur batteries, *Molecules*, 2021, **26**(9), 2507.
9 X. Xu, J. Wu, S. Ye, *et al.*, Sulfur/Iodine/Graphene Composites as a Cathode Material for Lithium–Sulfur Battery, *J. Electrochem. Soc.*, 2020, **167**(8), 080521.
10 L. P. Yu, L. Xu, C. Shearer, *et al.*, Solutions to the Challenges of Lithium–Sulfur Batteries by Carbon Nanotubes, *Adv. Sustainable Syst.*, 2023, **7**(7), 2300061.
11 N. Yahalom, L. Snarski, A. Maity, *et al.*, Durable lithium–sulfur batteries based on a composite carbon nanotube cathode, *ACS Appl. Energy Mater.*, 2023, **6**(9), 4511–4519.
12 W. Y. Lee, E. M. Jin, J. S. Cho, *et al.*, Freestanding flexible multilayered Sulfur–Carbon nanotubes for Lithium–Sulfur battery cathodes, *Energy*, 2020, **212**, 118779.
13 S. Qiu, J. Zhang, X. Liang, *et al.*, Tunable MOFs derivatives for stable and fast sulfur electrodes in Li-S batteries, *Chem. Eng. J.*, 2022, **450**, 138287.
14 C. Kensy, P. Härtel, J. Maschita, *et al.*, Scalable production of nitrogen-doped carbons for multilayer lithium-sulfur battery cells, *Carbon*, 2020, **161**, 190–197.
15 L. Zhao, L. Zhao, Y. Zhao, *et al.*, Nitrogen-sulfur dual-doped citric-acid porous carbon as host for Li-S batteries, *Alexandria Eng. J.*, 2022, **61**(7), 5343–5350.
16 R. Wu, S. Chen, J. Deng, *et al.*, Hierarchically porous nitrogen-doped carbon as cathode for lithium–sulfur batteries, *J. Energy Chem.*, 2018, **27**(6), 1661–1667.

17 J. G. Kim, Y. Noh and Y. Kim, Highly reversible lithium-sulfur batteries with nitrogen-doped carbon encapsulated sulfur cathode and nitrogen-doped carbon-coated ZnS anode, *Chem. Eng. J.*, 2022, **435**, 131339.
18 L. Zhao, L. Zhao, Y. Zhao, *et al.*, Nitrogen/sulfur dual-doped micro-mesoporous hierarchical porous carbon as host for Li-S batteries, *Front. Bioeng. Biotechnol.*, 2022, **10**, 997622.
19 I. Hussain, F. Bibi, S. Pandiyarajan, *et al.*, Partially oxidized MXenes for energy storage applications, *Prog. Mater. Sci.*, 2024, 101351.
20 X. Li, Z. Huang, C. E. Shuck, *et al.*, MXene chemistry, electrochemistry and energy storage applications, *Nat. Rev. Chem*, 2022, **6**(6), 389–404.
21 Y. Wu and M. Sun, Recent progress of MXene as an energy storage material, *Nanoscale Horiz.*, 2024, **9**(2), 215–232.
22 S. Bansal, P. Chaudhary, B. B. Sharma, *et al.*, Review of MXenes and their composites for energy storage applications, *J. Energy Storage*, 2024, **87**, 111420.
23 H. Yuan, J. Hua, W. Wei, *et al.*, Progress and prospect of flexible MXene-based energy storage, *Carbon Energy*, 2025, e639.
24 Z. Wu, Y. Zhao, Y. Li, *et al.*, Hybridization of MXene and covalent organic frameworks as electroactive materials for Li–S batteries and oxygen electrocatalysis, *Mater. Chem. Front.*, 2024, **8**(16), 2788–2801.
25 T. Wang, D. Luo, Y. Zhang, *et al.*, Hierarchically porous Ti3C2 MXene with tunable active edges and unsaturated coordination bonds for superior lithium–sulfur batteries, *ACS Nano*, 2021, **15**(12), 19457–19467.
26 Q. Liu, M. Wang, Y. Zhang, *et al.*, FeF3· 0.33 H2O nanoparticles decorated Ti3C2 MXene as high-performance bifunctional sulfur host for lithium-sulfur batteries, *J. Energy Storage*, 2024, **99**, 113401.
27 Q. Zhao, Q. Zhu, Y. Liu, *et al.*, Status and prospects of MXene-based lithium–sulfur batteries, *Adv. Funct. Mater.*, 2021, **31**(21), 2100457.
28 Y. X. Li, Y. S. Feng, L. X. Li, *et al.*, Green synthesis and applications of MXene for lithium–sulfur batteries, *Energy Storage Mater.*, 2024, **67**, 103257.
29 C. Shi, X. Zhang, Z. Li, *et al.*, Review and Perspectives on Preparation Strategies and Applications of Ti3C2 MXene for Li Metal Batteries/Li–S Batteries, *Energy Fuels*, 2024, **38**(16), 14866–14890.
30 D. R. Kumar, I. Kanagaraj, R. Sukanya, *et al.*, Ti3C2T x Filled in EMIMBF4 Semi-Solid Polymer Electrolytes for the Zinc–Metal Battery, *ACS Appl. Mater. Interfaces*, 2024, **16**(26), 33294–33306.
31 J. Li, Q. Jin, F. Yin, *et al.*, Effect of Ti 3 C 2 T x–PEDOT: PSS modified-separators on the electrochemical performance of Li–S batteries, *RSC Adv.*, 2020, **10**(66), 40276–40283.
32 X. Zhong, W. Yi, Y. Qu, L. Zhang, H. Bai, Y. Zhu, J. Wan, S. Chen, M. Yang, L. Huang, M. Gu, H. Pan and B. Xu, Co single-atom anchored on Co3O4 and nitrogen-doped active carbon toward bifunctional catalyst for zinc-air batteries, *Appl. Catal., B*, 2020, **260**, 118188.
33 R. Fang, K. Chen, L. Yin, Z. Sun, F. Li and H.-M. Cheng, The Regulating Role of Carbon Nanotubes and Graphene in Lithium-Ion and Lithium–Sulfur Batteries, *Adv. Mater.*, 2019, **31**, 1800863.
34 H. Ji, L. Tao, B. Hu, *et al.*, Enhanced rate and low-temperature performance of LiFePO4 cathode with 2D Ti3C2 MXene as conductive network, *J. Electroanal. Chem.*, 2023, **928**, 117047.
35 C. Qiao, H. Wu, X. Xu, *et al.*, Electrical conductivity enhancement and electronic applications of 2D Ti3C2Tx MXene materials, *Adv. Mater. Interfaces*, 2021, **8**(24), 2100903.
36 T. Guo, D. Zhou, S. Deng, *et al.*, Rational design of Ti3C2T x MXene inks for conductive, transparent films, *ACS Nano*, 2023, **17**(4), 3737–3749.
37 K. Han, T. Wang, N. Zhang, *et al.*, A film coating assembled by tubular nitrogen-doped carbon fibers as an efficient membrane spacer to suppress the shuttle effect for long-life lithium–sulfur batteries, *Electrochim. Acta*, 2021, **365**, 137232.
38 M. T. Li, J. Chen, K. Ren, *et al.*, Nitrogen and titanium-codoped porous carbon nanocomposites derived from metal–organic framework as cathode to address polysulfides shuttle effects by Ti-assisted N-inhibiting strategy, *RSC Adv.*, 2022, **12**(55), 35923–35928.
39 S. Singsen, I. Fongkaew, P. Hirunsit, *et al.*, Suppressing polysulfides shuttling and promoting sulfur utilization via transition metal and nitrogen Co-do** on graphdiyne cathodes of lithium-sulfur batteries: A first-principles modeling, *ACS Appl. Energy Mater.*, 2022, **5**(8), 9722–9732.
40 Y. Liu, X. Huang, H. Zhang, *et al.*, A bi-functional catalyst strategy to selectively regulate sulfur redox kinetics in lithium–sulfur batteries, *J. Mater. Sci. Technol.*, 2024, **173**, 54–62.
41 M. Zheng, Z. Luo, Y. Song, *et al.*, Carbon-coated nitrogen, vanadium co-doped MXene interlayer for enhanced polysulfide shuttling inhibition in lithium-sulfur batteries, *J. Power Sources*, 2023, **580**, 233445.
42 J. Song, X. Guo, J. Zhang, Y. Chen, C. Zhang, L. Luo, F. Wang and G. Wang, Rational design of free-standing 3D porous MXene/rGO hybrid aerogels as polysulfide reservoirs for high-energy lithium–sulfur batteries, *J. Mater. Chem. A*, 2019, **7**, 6507–6513.
43 S. A. Lateef, A. Raulo, J. Chmiola, *et al.*, Effect of Carbon Morphology and Slurry Formulation in Sulfur Cathode for Li-S Batteries, *J. Electrochem. Soc.*, 2024, **171**(12), 120518.
44 X. Zhong, W. Yi, Y. Qu, L. Zhang, H. Bai, Y. Zhu, J. Wan, S. Chen, M. Yang, L. Huang, M. Gu, H. Pan and B. Xu, Co single-atom anchored on Co3O4 and nitrogen-doped active carbon toward bifunctional catalyst for zinc-air batteries, *Appl. Catal., B*, 2020, **260**, 118188.
45 L. Wang, C. Yang, S. Dou, S. Wang, J. Zhang, X. Gao, J. Ma and Y. Yu, Nitrogen-doped hierarchically porous carbon networks: synthesis and applications in lithium-ion battery, sodium-ion battery and zinc-air battery, *Electrochim. Acta*, 2016, **219**, 592–603.
46 C. Kensy, P. Härtel, J. Maschita, *et al.*, Scalable production of nitrogen-doped carbons for multilayer lithium-sulfur battery cells, *Carbon*, 2020, **161**, 190–197.

47 F. Qu, Z. Yu, M. Krol, *et al.*, Electrochemical performance of carbon-rich silicon carbonitride ceramic as support for sulfur cathode in lithium sulfur battery, *Nanomaterials*, 2022, **12**(8), 1283.
48 Z. Luo, W. Lei, X. Wang, *et al.*, AlF3 coating as sulfur immobilizers in cathode material for high performance lithium-sulfur batteries, *J. Alloys Compd.*, 2020, **812**, 152132.
49 X. F. Liu, H. Chen, R. Wang, *et al.*, Cationic Covalent-Organic Framework as Efficient Redox Motor for High-Performance Lithium–Sulfur Batteries, *Small*, 2020, **16**(34), 2002932.
50 X. Tao, Y. Qi, Q. Gu, *et al.*, Ti3C2 QDs@ CNTs with Active Titanium Species as Bidirectional Catalytic Cathode for Facilitating Lithium Polysulfide Conversion in Li–S Batteries, *Adv. Funct. Mater.*, 2025, 2420532.
51 C. Shi, X. Zhang, Z. Li, *et al.*, Review and Perspectives on Preparation Strategies and Applications of Ti3C2 MXene for Li Metal Batteries/Li–S Batteries, *Energy Fuels*, 2024, **38**(16), 14866–14890.
52 J. Zhang, M. Xiao, W. Du, *et al.*, Co3V2O8 Composite Carbon Hollow Spheres Bidirectionally Catalyze the Conversion of Lithium Polysulfide to Improve the Capacity of Lithium-Sulfur Batteries, *Batteries Supercaps*, 2024, **7**(12), e202400310.
53 A. Hu, M. Zhou, T. Lei, *et al.*, Optimizing redox reactions in aprotic lithium–sulfur batteries, *Adv. Energy Mater.*, 2020, **10**(42), 2002180.
54 Q. Jin, K. Zhao, L. Wu, *et al.*, Enhancing Li cycling coulombic efficiency while mitigating "shuttle effect" of Li-S battery through sustained release of LiNO3, *J. Energy Chem.*, 2023, **84**, 22–29.
55 X. Qiu, Q. Hua, L. Zheng, *et al.*, Study of the discharge/charge process of lithium–sulfur batteries by electrochemical impedance spectroscopy, *RSC Adv.*, 2020, **10**(9), 5283–5293.
56 C. Liu, Z. J. Yin, H. Deng, *et al.*, Nitrogen-Doped Porous Carbon as High-Performance Cathode Material for Lithium-Sulfur Battery, *ChemistrySelect*, 2017, **2**(34), 11030–11034.
57 W. Bao, L. Liu, C. Wang, *et al.*, Facile synthesis of crumpled nitrogen-doped mxene nanosheets as a new sulfur host for lithium–sulfur batteries, *Adv. Energy Mater.*, 2018, **8**(13), 1702485.